Extraction of parton distribution functions using recent LHCb, ALICE and HERA heavy-flavour measurements

PROSA Collaboration

Abstract

The impact of measurements of heavy-flavour production in deep inelastic ep scattering and in pp collisions on parton distribution functions is studied in a QCD analysis at next-to-leading order. Recent combined results of inclusive and heavy-flavour production cross sections in deep inelastic scattering at HERA are investigated together with heavy-flavour production measurements at the LHC. Differential cross sections of charm- and beauty-hadron production measured by the LHCb collaboration at the center of mass energies of 5, 7 and 13 TeV as well as the recent measurements of the ALICE experiment at the center of mass energies of 5 and 7 TeV are explored. These data impose additional constraints on the gluon and the sea-quark distributions at low partonic fractions x of the proton momentum, down to $x \approx 10^{-6}$, which is the kinematic region of relevance for high-energy neutrino production. The impact of the resulting uncertainties in the nucleon composition, affecting predictions for the atmospheric prompt neutrino fluxes is presented.

1 Introduction

The fundamental structure of the nucleon is described by the theory of strong interactions, quantum chromodynamics (QCD). In the collinear factorisation, the nucleon structure is expressed in terms of parton distribution functions (PDFs), defined as probability densities for partons to carry a fraction x of the nucleon momentum at a factorisation scale μ_f. While the scale evolution of the PDFs is calculated in perturbative QCD (pQCD) and presented by the DGLAP equations [1–7], the x-dependence must be constrained using the experimental measurements. The constraining power of experimental data on particular parton distribution is to large extent defined by the acceptance of the experiment. Measurements of neutral current (NC) and charged current (CC) cross sections in deep inelastic scattering (DIS) at HERA probe the x-range of $10^{-4} < x < 10^{-1}$, impose most significant constraints on the light quark PDFs and probe the gluon distribution via scaling violations. Additional constraints on the flavour separation of the quark sea and on the gluon distribution at low and high x are obtained by using the measurements at fixed target experiments and in proton-(anti)proton collisions. Heavy-flavour production in proton-proton collisions at the LHC is dominated by the gluon-gluon fusion, therefore corresponding measurements probe the gluon distribution directly. The measurements of forward charm [8] and beauty [9] production by the LHCb experiment at the center-of-mass energy $\sqrt{s} = 7$ TeV were used for the first time by the PROSA collaboration [10] to improve constraints on the gluon distribution at $5 \times 10^{-6} < x < 10^{-4}$, in the region not covered by any other data to that date. The resulting PDFs were further used to investigate the uncertainties in the predictions of prompt neutrino fluxes in the atmosphere [11].

Recent improvements in precision of HERA measurements, new experimental data on heavy flavour production at the LHC at different $\sqrt{s}$, together with new developments in the theory and improvements of the phenomenological tools, offer possibilities for stronger constraints on the gluon distribution at low x. These improvements in experimental measurements and the theory are explored in the QCD analysis presented in this paper, which updates the earlier result [10]. The results are used in the predictions for the prompt atmospheric neutrino fluxes.

2 Input data sets and used theory predictions

The main objective of the present QCD analysis is to demonstrate the constraining power of the updated measurements of heavy-flavour production in DIS and proton-proton collisions for the determination of the PDFs of the proton. The QCD analysis is performed at next-to-leading order (NLO) using the xFitter framework [12]. The updated combinations of the inclusive DIS cross sections [13] and of charm and beauty production cross sections [14] are used together with the measurements of charm and beauty hadroproduction in proton-proton scattering at the LHC. The latter include the measurements of charm hadroproduction by the LHCb collaboration at 5 TeV [15], 7 TeV [8] and 13 TeV [16], and by ALICE at 5 TeV [17] and 7 TeV [18]. The measurements of beauty hadroproduction by the LHCb at 7 TeV [9] are also used.

The cross sections measured by the LHCb and ALICE in each p_T range are normalized in rapidity y, $\frac{d^2\sigma}{dydp_T} / (\frac{d^2\sigma}{dydp_T})_0$. Here, $\left(\frac{d^2\sigma}{dydp_T}\right)_0$ is the cross section in the central LHCb rapidity bin, $3 < y < 3.5$. Note that ALICE measurements at $|y| < 0.5$ are normalised to the LHCb cross section

measurement in $3 < y < 3.5$. The advantage of using the normalised cross section, demonstrated in the earlier PROSA analysis [10], is a significant reduction of the scale dependence in the theoretical prediction, while retaining the sensitivity to the PDFs.

In the presented QCD analysis, bin-to-bin correlations in the input measurements are taken into account as described in the following. The treatment of correlated experimental uncertainties for the HERA data follows that of the original publications [13, 14].

The correlated uncertainties in the ALICE and LHCb measurements reported in original publications [8, 9, 15–18] and listed in the respective tables as exact uncertainty values in each kinematic bin in p_T and y, are treated as fully correlated, and the uncorrelated uncertainties are obtained by subtracting the correlated ones from the total uncertainties, in quadrature. The systematic uncertainties, reported as error intervals, see e.g. Table (2) of [15], are assumed uncorrelated, since no details about their size in individual p_T and y bins are provided. Because of this treatment of systematics, most of the correlated systematic uncertainties cancel in the calculation of the normalised cross sections. In case of the LHCb cross section ratio measurements, the uncertainties cancel completely. For different final state measurements within one experiment, the tracking and luminosity uncertainties are treated as correlated. Furthermore, all experimental uncertainties are treated as uncorrelated among measurements at different center-of-mass energies. The uncorrelated uncertainties in the normalized cross sections $\frac{d\sigma}{dy_0}$ are propagated as correlated uncertainties to the respective complementary rapidity bins. It is worthwhile to note, that the details of the experimental uncertainties and their correlations in each individual kinematic range is of great importance and therefore most detailed information about the systematic correlations in the experimental measurement is required.

In the presented QCD analysis, the scale evolution of partons is calculated through DGLAP equations at NLO, as implemented in the QCDNUM programme [19]. The description of HERA data in PDF fits at next-to-next-to-leading order (NNLO) improves in the kinematic range of small x and low Q^2, by including higher twist effects [20, 21] or, alternatively, small x resummation [22, 23]. These upgrades are left for future analyses, once all necessary theoretical ingredients have become available.

The theoretical FFNS predictions for the heavy-quark and inclusive HERA data are obtained using OPENQCDRAD [19] code in the fixed-flavour-number scheme (FFNS) with the three active flavours in the proton, following the Ref. [14]. Similar to the earlier PROSA analysis [10], the theoretical predictions for the fully differential heavy-quark hadroproduction in proton-proton collisions, available at NLO in FFNS, are used. These are calculated using the MNR code, with the single-particle inclusive distributions computed using the pole mass scheme for the heavy quarks, and translated into the $\overline{\text{MS}}$ scheme expressions using the $\overline{\text{MS}}$ mass $m_Q(m_Q)$ and following the Ref. [24]. The $\overline{\text{MS}}$ mass scheme is then consistently used in the calculations for all used processes.

The factorisation and renormalisation scales are chosen to be Q for the inclusive DIS, and $\mu_r = \mu_f = \sqrt{Q^2 + 4m_Q(m_Q)^2}$ for the heavy quark production in DIS, respectively, with $m_Q(m_Q)$ representing the heavy-quark mass in the $\overline{\text{MS}}$ scheme. For heavy quark production in proton-proton collision, $\mu_r = \mu_f = \sqrt{4m_Q(m_Q)^2 + p_T^2}$ is assumed.

The calculations for the heavy quark hadroproduction are supplemented with phenomeno-

2

logical non-perturbative fragmentation functions to describe the transition of heavy quarks into hadrons. The fragmentation of charm quarks into D-mesons is described by the Kartvelishvili function $D_Q(z) \propto z^{\alpha_K}(1-z)$ with $\alpha_K = 4.4 \pm 1.7$ as measured at HERA [25, 26], and for the fragmentation of beauty quarks $\alpha_K = 11 \pm 3$ is used as measured at LEP [27], following the previous PROSA analysis [10]. Studies of the uncertainties related to the fragmentation in [28] for a determination of the charm-quark mass in the $\overline{\text{MS}}$ scheme from deep inelastic scattering at HERA data have shown that the dominant effect is captured by varying α_K within its uncertainties. This treatment of charm quark fragmentation is independent of choice of a particular renormalization scheme for the heavy quark mass. The latter is needed in a determination of the initial condition for the perturbative heavy quark fragmentation function, which is known to NNLO [29]. The subsequent range of evolution in the case of charm quark fragmentation into D-mesons from the scale of hadronisation to scales of order of the charm quark mass is very short, so that the modeling with the non-perturbative Kartvelishvili function $D_Q(z)$ is justified.

The main QCD analysis is performed in the FFNS and the sensitivity of the heavy quark measurements to the PDFs and to the masses of the charm and beauty quarks is fully explored by treating $m_c(m_c)$ and $m_b(m_b)$ as free parameters in the fit. The fit is also performed in the variable flavour number scheme (VFNS) to allow for possible applications of the results in the LHC analyses, e.g. tuning of the underlying event in the Monte Carlo simulations.

3   PDF parametrisation

The PDFs are parametrised at the starting evolution scale of $\mu_{f0}^2 = 1.9\,\text{GeV}^2$, similar as in Ref. [13] and Ref. [30], as follows:

$$
\begin{aligned}
xg(x) &= A_g x^{B_g} (1-x)^{C_g} (1 + F_g \log x), \\
u_{\text{v}}(x) &= A_{u_{\text{v}}} x^{B_{u_{\text{v}}}} (1-x)^{C_{u_{\text{v}}}} (1 + E_{u_{\text{v}}} x^2), \\
d_{\text{v}}(x) &= A_{d_{\text{v}}} x^{B_{d_{\text{v}}}} (1-x)^{C_{d_{\text{v}}}}, \\
x\overline{\text{U}}(x) &= A_{\overline{\text{U}}} x^{B_{\overline{\text{U}}}} (1-x)^{C_{\overline{\text{U}}}} (1 + D_{\overline{\text{U}}} x), \\
x\overline{\text{D}}(x) &= A_{\overline{\text{D}}} x^{B_{\overline{\text{D}}}} (1-x)^{C_{\overline{\text{D}}}}.
\end{aligned}
\tag{1}
$$

Here, $xg(x)$, $xu_{\text{v}}(x)$ and $xd_{\text{v}}(x)$ represent the gluon, up and down valence quark distributions, respectively. The sea quark distribution is defined as $x\Sigma(x) = x\overline{u}(x) + x\overline{d}(x) + x\overline{s}(x)$, with $x\overline{u}(x)$, $x\overline{d}(x)$, and $x\overline{s}(x)$ denoting the up, down, and strange antiquark distributions, respectively. For the up- and down-type antiquark distributions, $x\overline{\text{U}}(x)$ and $x\overline{\text{D}}(x)$, relations $x\overline{\text{U}}(x) = x\overline{u}(x)$ and $x\overline{\text{D}}(x) = x\overline{d}(x) + x\overline{s}(x)$ are assumed. The normalisation parameters $A_{u_{\text{v}}}$, $A_{d_{\text{v}}}$, and A_g are determined by the QCD sum rules. The strangeness fraction $f_s = x\overline{s}/(x\overline{d} + x\overline{s})$ is fixed to $f_s = 0.4$ as in the HERAPDF2.0 analysis [13]. Additional constraints $B_{\overline{\text{U}}} = B_{\overline{\text{D}}}$ and $A_{\overline{\text{U}}} = A_{\overline{\text{D}}}(1 - f_s)$ are imposed to ensure the same normalisation for the $x\overline{u}$ and $x\overline{d}$ distributions as $x \to 0$. The term $F_g \log x$ was proposed in [30] to provide a more flexible functional form at low x.

The predicted and measured cross sections together with their corresponding uncertainties are used to build a global χ^2, minimized to determine the initial PDF parameters. The χ^2 definition

3

follows that of Eq. (32) in Ref. [13]. In the minimisation, performed using the MINUIT package [31], the experimental uncertainties in the heavy-quark normalised cross sections are treated as additive, and the treatment of the experimental uncertainties for the HERA DIS data follows the prescription given in Ref. [13].

The parameters in Eq. (1) are selected by first parametrising each PDF as

$$xf(x) = Ax^B(1-x)^C(1 + Dx + Ex^2) \tag{2}$$

with all D and E parameters set to zero. The other parameters are then included in the fit one at a time. The improvement in χ^2 of the fits is monitored and the procedure is stopped when no further improvement is observed. The inclusion of the F_g parameter does not lead to sizable change in χ^2, in particular, its fitted value is consistent with 0 within uncertainty, however the variation of F_g significantly affects the fit uncertainties. To ensure that the gluon PDF at low x is not overconstrained in the fit, different functional forms in the parametrisation were tested, as used in the ABMP16 [21], CT14 [32], HERAPDF2.0 [13], MMHT2014 [33] and Bonvini-Giuli (BG) [30] PDF fits. The details of this study are given in Appendix, see Section A.

4 PDF uncertainties

The PDF uncertainties are investigated according to the general approach of HERAPDF2.0 analysis [13], with the fit, model, and parametrisation uncertainties taken into account.

The fit uncertainties arising from the uncertainties in the measurements are estimated by using the Hessian method [34], adopting the tolerance criterion of $\Delta\chi^2 = 1$ and correspond to 68% confidence level.

To investigate the impact of model assumptions on the resulting PDFs, alternative fits are performed and the differences to the central result are considered as model uncertainties. The strangeness fraction is varied as $0.3 \leq f_s \leq 0.5$ and the value of $Q^2_{\min}$ imposed on the HERA data as $2.5 \leq Q^2_{\min} \leq 5.0 \text{GeV}^2$. The FFNS strong coupling constant is assumed as $0.105 < \alpha_s^{n_f=3}(M_Z) < 0.107$ (corresponding to the VFNS values of $0.117 < \alpha_s^{n_f=5}(M_Z) < 0.119$ [35]). The variation of the fragmentation parameters $\alpha_K = 4.4 \pm 1.7$ for charm hadrons and $\alpha_K = 11 \pm 3$ for beauty hadrons is performed. The scales μ_f and μ_r for heavy quark production are varied independently and simultaneously up and down by a factor of two, excluding variations of the two scales in opposite directions. Note that for the normalized cross section predictions, the simultaneous variation of the μ_f and μ_r scales in the same direction results in the largest deviation in the resulting PDFs and is considered as one PDF uncertainty eigenvector.

The parametrisation uncertainty is estimated by extending the functional form of each PDF in Eq. (1) with additional parameters D and E, see Eq. (2), which are added or removed one at a time and do not impact the χ^2. In particular, the shape of the gluon PDF is extended by adding the $+G_g \log^2 x$ term [30]. This modification does not result in an improvement in χ^2 and therefore is not considered in the nominal parametrisation. The variation of the starting scale, $1.6 < \mu_{f0}^2 < 2.2 \text{ GeV}^2$, is also taken into account as contribution to the parametrisation uncertainty. The parametrisation uncertainty is constructed as an envelope built from the maximal differences

4

between the PDFs resulting from all the parameterization variations and the central fit at each x value.

The total PDF uncertainty is obtained by adding experimental, model, and parameterization uncertainties in quadrature.

5   Results

The quality of the overall fit can be judged based on the global χ^2 divided by the number of degrees of freedom, n_{dof}. For each data set included in the fit, a partial χ^2 divided by the number of measurements (data points), n_{dp}, is provided. The correlated part of χ^2 quantifies the influence of the correlated systematic uncertainties in the fit. The global and partial χ^2 values for each data set are listed in Table 1, illustrating a general agreement among all the data sets. The central values and the uncertainties of the fitted parameters are given in Table 2.

The fitted PDFs with their total uncertainties at the scale $\mu_f^2 = 10 \text{ GeV}^2$ are shown in Fig. 1. These are compared to the result of the PROSA 2015 fit [10]. In Fig. 2 (left), the gluon distribution normalised to the one from the PROSA 2015 fit is shown. The two results are in a very good agreement and a significant improvement in the precision of the gluon PDF is achieved at $x < 10^{-4}$, as compared to the PROSA 2015 fit. The valence and sea quark PDFs are in good agreement with the result of HERAPDF2.0 analysis [13] and the observed differences in these distributions to the PROSA 2015 analysis are attributed to the update of the DIS measurements [36] used in Ref. [10] to the final combination [13] of the HERA data.

The relative total, fit, model and parametrisation uncertainties for the gluon PDF are shown in Fig. 2 (right). The total uncertainties are dominated by the model uncertainties, with the largest contributions arising from the scale variations in predictions for heavy-quark hadroproduction. Reduction of these uncertainties would require theoretical calculations at higher order.

The resulting PDFs are available in the LHAPDF format at [...].

5.1   Fit in VFNS

The fit in the VFNS is performed using the APFEL library [37] interfaced in xFitter. The theoretical predictions for the HERA data are computed using the FONLL-B scheme [38] with the pole charm and beauty quark masses set to $m_c^{\text{pole}} = 1.4 \text{ GeV}$ and $m_c^{\text{pole}} = 4.5 \text{ GeV}$ respectively. However, no VFNS calculation for heavy-quark hadroproduction is interfaced to public tools and can be used for PDF fitting. To keep using the MNR calculations with the VFNS, we exploit the feature of the APFEL library to choose arbitrary heavy-quark matching thresholds [39]. These thresholds are set to values:

$$\mu_c = 4.5 m_c^{\text{pole}} = 6.3 \text{ GeV},$$
$$\mu_b = 4.5 m_b^{\text{pole}} = 20.25 \text{ GeV}. \tag{3}$$

We imposed kinematic cuts $p_T < 5$ GeV and $p_T < 16$ GeV on the LHC charm and beauty data, respectively, to ensure that we are working with not more than 3 (4) light flavours when calculating predictions for charm (beauty) data. The strong coupling strength is set to $\alpha_s^{n_f=5}(M_Z) = 0.118$ [35],

Dataset	χ^2/ndp
HERA CC e^+p	62 / 39
HERA CC e^-p	49 / 42
HERA NC e^-p	227 / 159
HERA NC e^+p 820 GeV	68 / 70
HERA NC e^+p 920 GeV	440 / 377
HERA NC e^+p 460 GeV	223 / 204
HERA NC e^+p 575 GeV	223 / 254
HERA NC charm	49 / 52
HERA NC beauty	18 / 27
LHCb 7 TeV B^0	52 / 76
LHCb 7 TeV B^+	129 / 108
LHCb 7 TeV B_s^0	37 / 60
LHCb 7 TeV D^0	15 / 30
LHCb 7 TeV D^+	19 / 29
LHCb 7 TeV D_s^+	14 / 20
LHCb 7 TeV D^{*+}	16 / 22
LHCb 5 TeV D^0	60 / 35
LHCb 5 TeV D^+	25 / 35
LHCb 5 TeV D_s^+	30 / 29
LHCb 5 TeV D^{*+}	35 / 30
LHCb 13 TeV D^0	111 / 60
LHCb 13 TeV D^+	72 / 64
LHCb 13 TeV D_s^+	69 / 55
LHCb 13 TeV D^{*+}	82 / 54
ALICE 7 TeV D^0	5.1 / 8
ALICE 7 TeV D^+	0.75 / 7
ALICE 7 TeV D^{*+}	2.3 / 6
ALICE 5 TeV D^0	6.3 / 10
ALICE 5 TeV D^+	5.8 / 9
ALICE 5 TeV D_s^+	2.5 / 4
ALICE 5 TeV D^{*+}	1.7 / 9
Correlated χ^2	282
Log penalty χ^2	-32
Total χ^2 / dof	2401 / 1969

Table 1: The global and partial χ^2 values for each data set together with the corresponding number of data points (ndp). The correlated χ^2 and the log penalty χ^2 entries refer to the χ^2 contributions from the correlated uncertainties and from the logarithmic term, respectively, as described in Ref. [13].
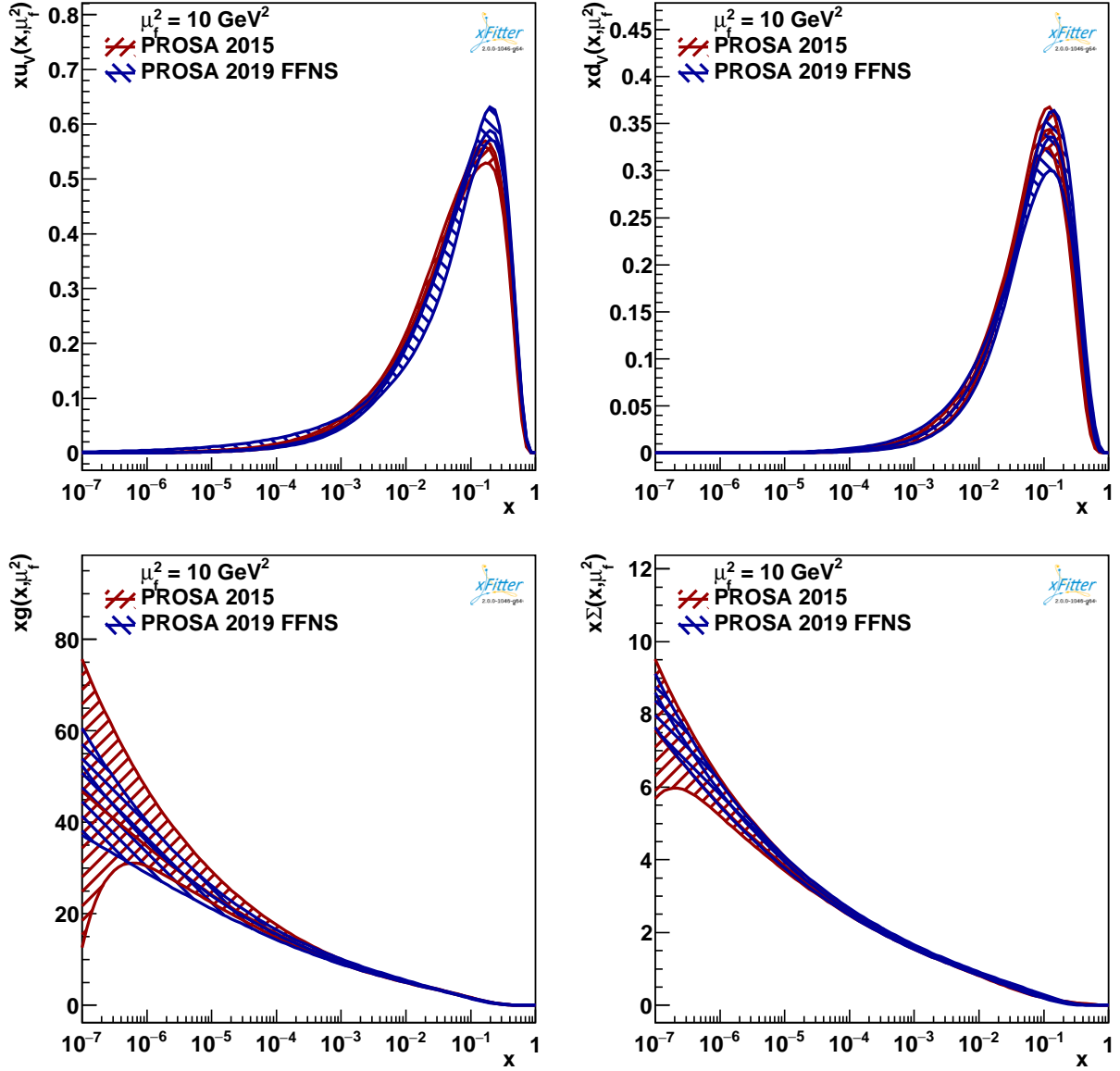
Figure 1: The fitted PDFs with their total uncertainties at the scale $\mu_f^2 = 10 \text{ GeV}^2$ compared with the distributions from the PROSA 2015 fit.

Parameter	Value
B_g	0.004 ± 0.053
C_g	6.25 ± 0.29
Fg	0.068 ± 0.024
B_{u_v}	0.644 ± 0.030
C_{u_v}	4.862 ± 0.076
E_{u_v}	15.8 ± 2.2
B_{d_v}	0.873 ± 0.076
C_{d_v}	4.61 ± 0.35
$C_{\overline{U}}$	7.36 ± 0.77
$D_{\overline{U}}$	10.1 ± 2.4
$A_{\overline{D}}$	0.1061 ± 0.0058
$B_{\overline{D}}$	-0.1661 ± 0.0062
$C_{\overline{D}}$	12.7 ± 3.0
$m_c(m_c)$	1.230 ± 0.031 GeV
$m_b(m_b)$	3.977 ± 0.100 GeV

Table 2: The resulting parameters for the PDFs with their fit uncertainties.
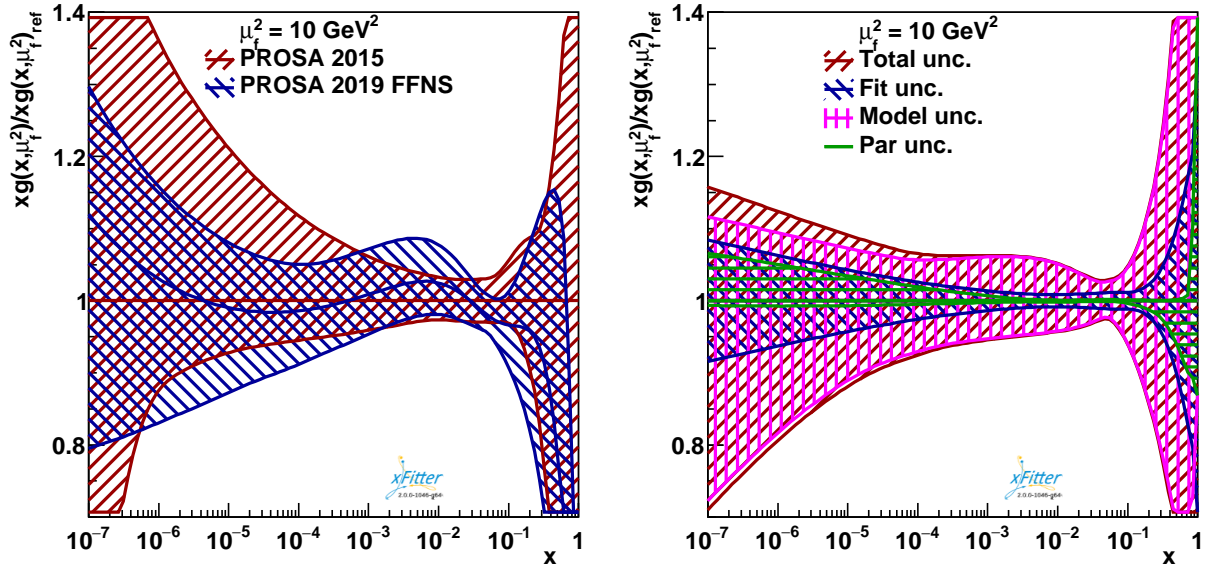
Figure 2: (left) The gluon PDF with their total uncertainties at the scale $\mu_f^2 = 10$ GeV^2 divided by the gluon PDF from the PROSA 2015 fit. (right) The relative total, fit, model and parametrisation uncertainties for the gluon PDF at the scale $\mu_f^2 = 10$ GeV^2.

while all other settings are the same as in the FFNS fit. The specific matching thresholds in Eq. (3) are chosen to ensure that a sufficient amount of the LHC charm and beauty data is still included in the fit. The choice of the matching thresholds is arbitrary and amounts to a renormalisation scheme choice [39], therefore we have verified that the fit results are stable under variations within $3.1 \leq \mu_Q/m_Q^{\text{pole}} \leq 6$, with the p_T cuts on the charm and beauty LHC data modified accordingly.

In this fit, $\chi^2 = 2114$ is obtained for $n_{dof} = 1714$, indicating a similar quality of data description as compared to the fit in the FFNS. The resulting PDFs are available in the LHAPDF format at [...]. No PDF uncertainties are provided with this set.

The performance of the new PDFs presented here was tested by computing predictions for the inclusive and multi-jet production in DIS [40–44] and jet [45] and top quark-antiquark production [46, 47] in proton-proton collisions. The variant of the presented PDFs is used. The results are found similar to those using HERAPDF2.0 PDF.[1]

---

[1]The resulting predictions compared to the measurements by H1, ZEUS and CMS experiments will be put on the PROSA webpage for reference.

6 Predictions for prompt atmospheric neutrino fluxes

Various applications in high-energy astroparticle physics could benefit from accurate PDFs in the low-x region. One of the most interesting cases is the evaluation of the atmospheric flux of prompt neutrinos, originating from the semileptonic decays of heavy-flavoured hadrons produced in the interactions of cosmic rays (CR) with nuclei in the atmosphere. The prompt atmospheric neutrino flux represents the main background for searches of highly energetic cosmic neutrinos, which are supposed to be produced in the vicinity of far astrophysical sources and in the Galactic Plane [48]. Such searches are conducted at Very Large Volume Neutrino Telescopes such as ANTARES [49], IceCube [50] and KM3NeT [51], which register and analyze the features of the track and cascade events induced by the charged-current and neutral-current weak interactions of the impinging neutrinos with the water/ice nuclei. To date, no direct measurement of the prompt atmospheric neutrino flux is available. Therefore, the most precise theoretical predictions for these fluxes are needed for the reliable interpretation of the experimental data in order to disentangle the cosmic neutrino component from the atmospheric background [52].

In this paper, the predictions for the prompt atmospheric neutrino fluxes are calculated, in general following the method detailed in Ref. [11]. It is assumed, that pA and AA interactions leading to charm production can be described in terms of pp interactions in pQCD (superposition model). In the present calculation, the proton structure is described by the new PROSA fit, referred to as PROSA19. Production and decay of the $D^{\pm}, D^0, \bar{D}^0, D_s^{\pm}, \Lambda_c^{\pm}$ in the atmosphere is considered dominant, since the contribution of other charmed hadrons, as well as b-flavoured hadrons, amounts to 5-15% of the dominant one [53]. In the computation of charmed-hadron production cross sections, the renormalization and factorization scales are chosen as $\mu_R = \mu_F = \mu_0 = \sqrt{p_T^2 + 4m_c^2}$, consistent with the scale choice adopted in the theory predictions of D- and B-meson production at LHCb and ALICE used in the PDF fit. Note that this scale choice differs from the one of Ref. [11], where $\mu_R = \mu_F = \sqrt{p_T^2 + m_c^2}$ was used, consistent with [10]. While the difference between the two scale choices reduces with increasing p_T, at low p_T, the present scale choice is motivated by faster convergence of the perturbative series to NNLO for the total $pp \rightarrow c\bar{c} + X$ cross section, as reported in Ref. [54].

In the present work, the central value of the pole mass of the charm quark, $m_c^{pole} = 1.43$ GeV is used, corresponding to $m_c(m_c) = 1.23$ GeV in the PDF fit (see Table 2), as obtained using 1-loop conversion. It is worthwhile to note that this value is larger then the one used in Ref. [11]. The uncertainty due to the choice of the charm quark mass is evaluated by varying the pole mass by $\pm$ 0.15 GeV around the central value.

The PDF uncertainties are evaluated using the 40 PROSA19 uncertainty eigenvectors, accounting for the contributions due to the fit, model, and the parameterization assumptions. These contributions are then summed up in quadrature. The uncertainty related to the choice of the scales is evaluated considering the envelope of the resulting cross section for the assumptions $\mu_R, \mu_F = \{(1, 1), (0.5, 0.5), (2, 2), (1, 2), (2, 1), (1, 0.5), (0.5, 1)\}$ (μ_0, μ_0) in the calculation.

The predictions for the prompt $(\nu_\mu + \bar{\nu}_\mu)$ fluxes are presented in in Fig. 3. Those are obtained by using different hypotheses for the primary CR all-nucleon flux [55, 56], which are derived from the measured CR all-particle spectrum, under specific assumptions for the CR composition. The

10

QCD uncertainties in the resulting prompt $(\nu_\mu + \bar{\nu}_\mu)$ fluxes encompass the uncertainties in the charm quark mass, PDF and those related to the scale choice, with the latter being the dominant uncertainty. As expected, the charm quark mass uncertainty decreases with energy: at small $E_{\nu,lab}$ it dominates over the PDF uncertainty, whereas at $E_{\nu,lab} \sim 10^7$ - 10^8 GeV, both uncertainty contributions become similar. At high $E_{\nu,lab}$, the PDF uncertainties are reduced with respect to those of Ref. [11], due to inclusion of more data sensitive to the low x region in the presented PDF PDF fit. The different contributions of the PDF uncertainty are shown in Fig. 4. All these contributions increase with increasing $E_{\nu,lab}$, which corresponds to the decreasing x of the involved partons, probed.

It is worthwhile to note, that the PDF uncertainties for $E_{\nu,lab} = 10^6$ - 10^8 GeV are calculated, assuming the PDFs can be extrapolated to x-values lower than the kinematic reach of the data used in the PDF fit, $x \approx 10^{-6}$. To date, there are no further measurements probing the x-range lower than 10^{-6} which would correspond to the highest neutrino energies, which can be accessed [57]. However, the result based on PROSA19 PDFs reaching the lower x values, remains consistent with the one based on PROSA15 PDF set. This fact can be considered as a consistency test of the extrapolation procedure, assuming no New Physics contribution in the probed x-range. Furthermore, at the neutrino energies of $E_{\nu,lab} \gtrsim 10^5$ GeV, the assumption on CR composition becomes very important (see Fig. 3), having an impact on both the shape and the normalisation of the prompt atmospheric neutrino flux.

In Fig. 5, the flux predictions using PROSA19PDF are compared to those using PROSA15, ABM11 and CT14 PDF sets. The predictions have been obtained using as a basis matrix-elements for $c\bar{c}$ hadroproduction at NLO in FFNS, matched, according to the Powheg formalism [58, 59], to the PYTHIA8 Parton Shower and Hadronization algorithms [60]. The proton structure is described by the PDFs with three active flavours with the corresponding values of $\alpha_S(M_Z)$. The predictions using PROSA19 PDF at high energies are slightly smaller than those using PROSA15 and ABM12 PDFs, due to a somewhat suppressed gluon at low x. Furthermore, in Fig. 5, the predictions obtained in the GM-VFNS framework of Ref. [61], using as input VFNS PDFs (CT14nlo and the PROSA19VFNS) are shown. The NLO QCD corrections are included in the partonic cross section, whereas the transition from partons to hadrons is described by fragmentation functions evolving with the factorization scale [62], a procedure which resums logarithms of p_T/m_c at next-to-leading-logarithmic accuracy. The central predictions using the GM-VFNS are compatible among each other, but show shape differences with respect to the FFNS ones. Part of these differences are related to the different treatment of the transition of partons into hadrons (parton shower + hadronization on the one hand, vs. fragmentation functions on the other hand). Also, a different factorization scale is used in the GM-VFNS predictions [2]. For comparison, the upper limit on the prompt neutrino flux obtained in the ICECube analysis [63] of up-going muons from the northern hemisphere is also shown and is well described by the predictions.

In Fig. 6 the presented flux prediction is compared to those obtained by other groups. In general, all the flux predictions are consistent within the uncertainties. The result of Ref [64] shows largest differences with the presented result due to using the charm cross section calculation at LO only. The ERS dipole model prediction [65], that is mostly used by the experimental collaborations

---

[2]Motivations for the specific $\mu_F = \mu_R/2$ choice adopted in the GM-VFNS computation are reported in Ref. [61]

in their data analysis, is also consistent with the prediction of this paper, within uncertainties. The uncertainties in the ERS prediction are smaller compared to the QCD-based prediction, however the way of the uncertainty accessment in both calculations can not be directly compared. Indeed the dipole approach is expected to effectively resum logarithmic contributions of the form $\alpha_S \ln(1/x)$ in the PDF evolution, a property which could lead to a reduction of the PDF uncertainties associated to the target parton at low x, whereas the resummation of these logarithms is not included in the DGLAP evolution. The uncertainties associated to the projectile parton PDFs in Ref [65] were estimated by comparing two different central PDF sets, without considering the PDF uncertainty associated to each of those. Furthermore, the factorization scale variation in Ref. [65] is performed in a limited range of $\mu_F = m_c$, $\mu_F = 2\, m_c$.

In Fig. 7, the prediction for the prompt neutrino flux based on the superposition model for both the projectile CR and the target nucleon of the air, obtained using the PROSA19 PDF set, is compared to the calculation of Ref. [53] which uses nuclear PDFs to describe the target nucleon (nitrogen) and the proton PDFs for the projectile CR. Both predictions agree well with each other.
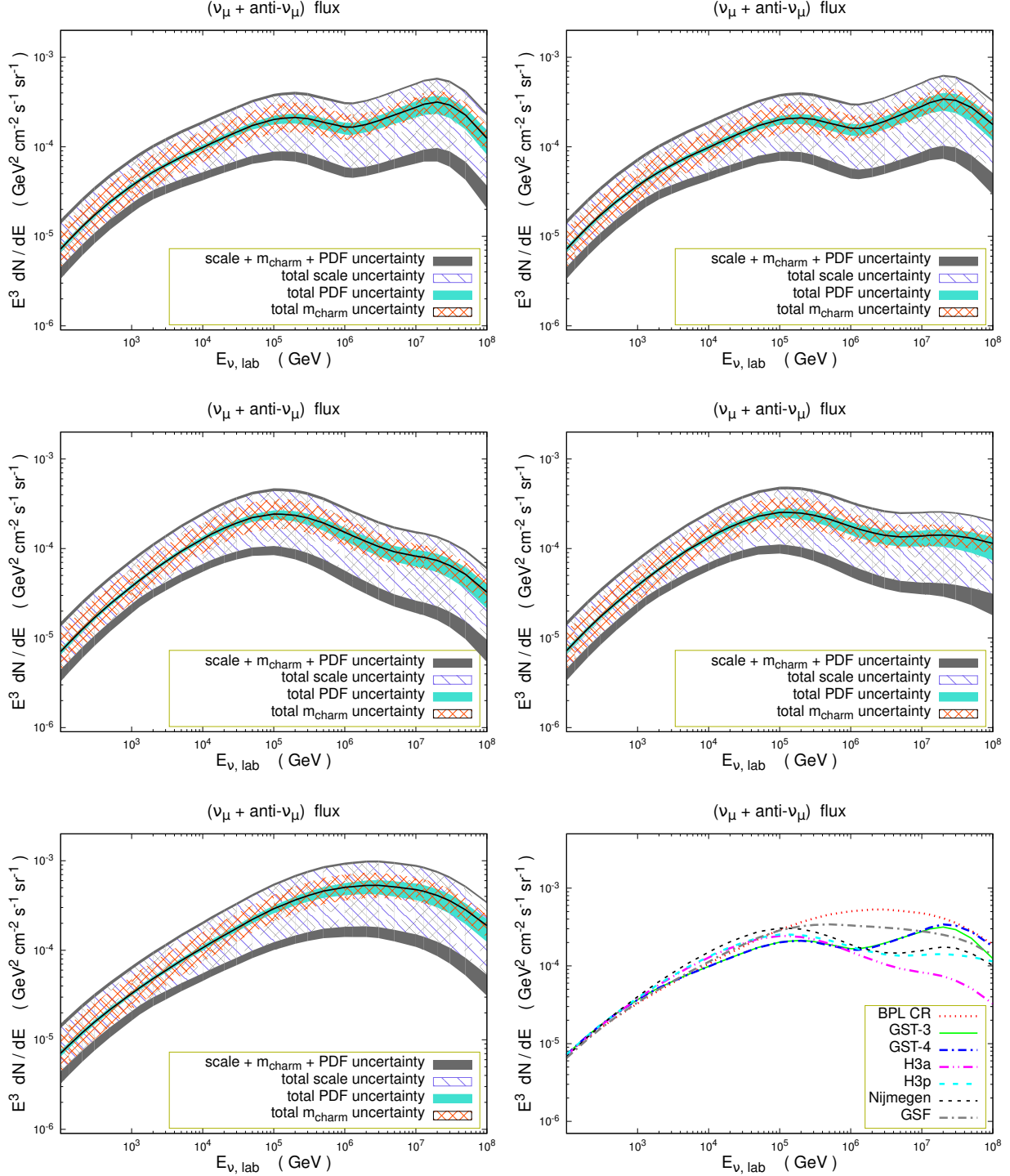
7 Summary

Acknowledgments

Figure 3: Prompt neutrino fluxes and their uncertainties related to scale, charm mass and PDF variation. Each panel refers to a different CR primary all-nucleon spectrum (GST-3, GST-4, H3p, H3a and BPL) [55, 56], chosen among those most widely used in literature. In the last panel the central predictions using all these primary all-nucleon spectra, together with those obtained with the more recently introduced Nijmegen [66] and GSF [67] all-nucleon spectra, are compared among each other.
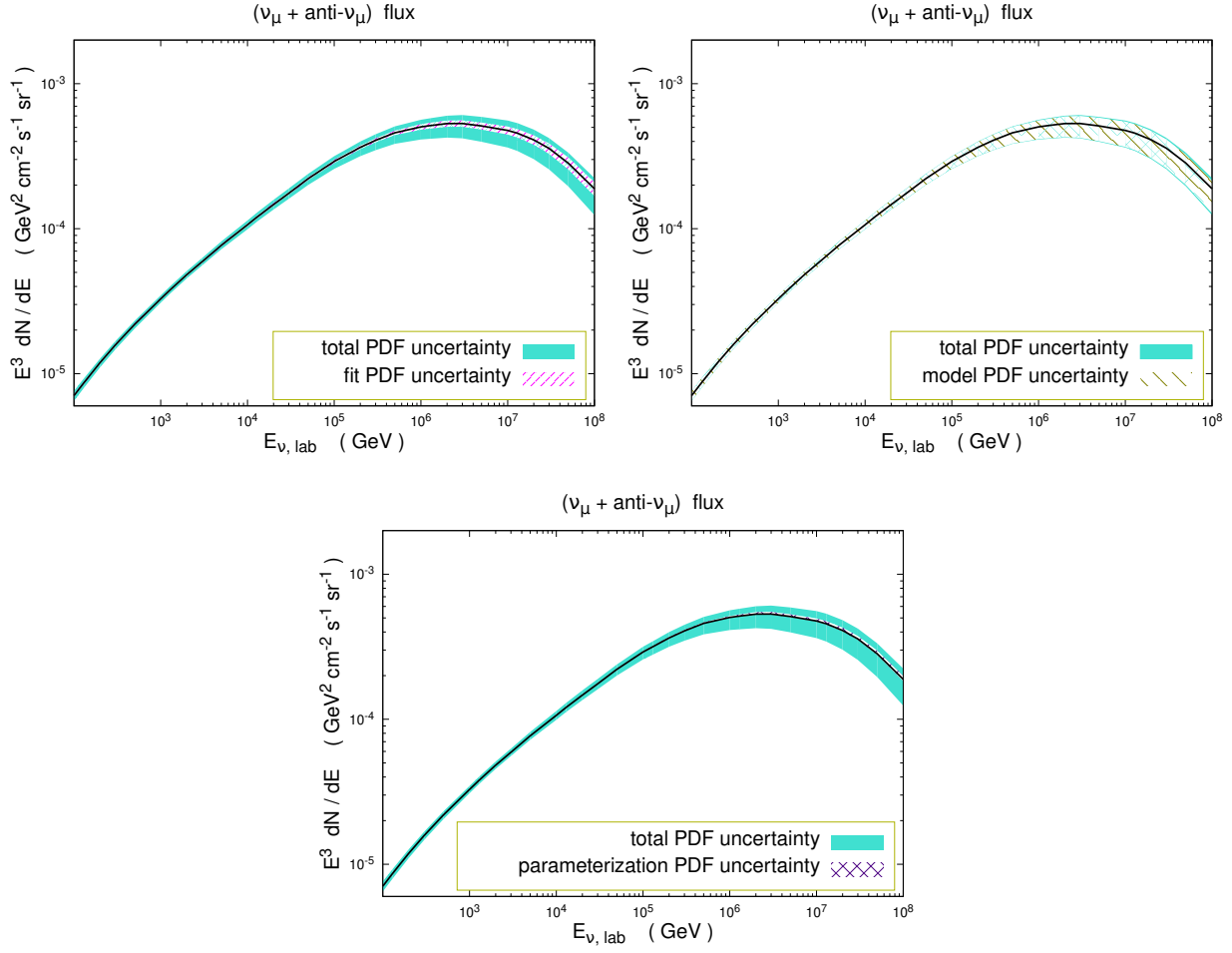
13

Figure 4: Contributions of the fit, model and parameterization uncertainties to the total PDF uncertainties on prompt neutrino flux. The BPL primary CR all-nucleon spectrum is used as input for the calculation.
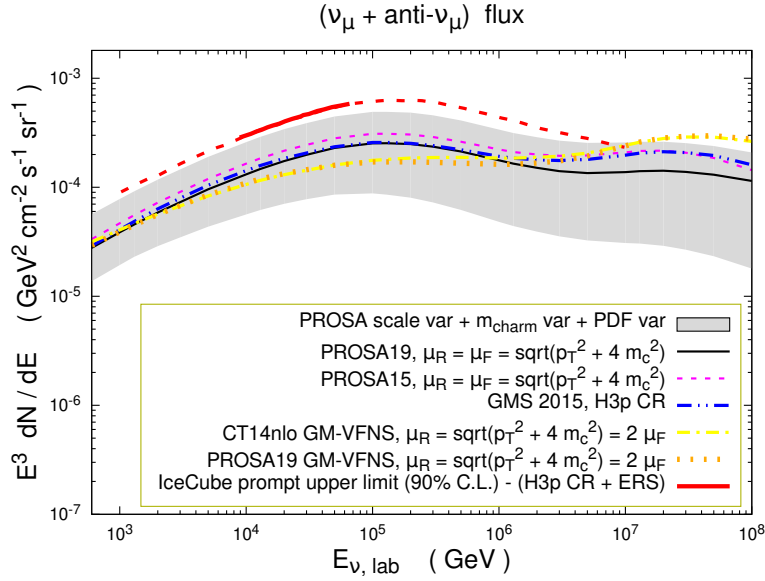
Figure 5: Predictions for prompt neutrino fluxes from this paper as compared to other predictions by our group. Predictions obtained with the PROSA PDF fit of Ref. [10], using the same $\mu_R = \mu_F$ scale, but a slightly different charm mass value ($m_c = 1.4$ GeV) are shown by dotted (pink) lines; the predictions of Ref. [54], using the ABM11 PDF fit [68], are shown by double-dotted-dashed (blue) lines. Finally the predictions using the VFNS version of the PDF fit described in this paper (see Section 5.1), in association with a GM-VFNS calculation of charm hadroproduction [61], are also reported and compared to those of Ref. [61] itself, that made use of the CT14nlo PDF fit [32]. The experimental upper limit on prompt ($\nu_\mu + \bar{\nu}_\mu$) flux, extracted from IceCube in the analysis of Ref. [63] is also reported.
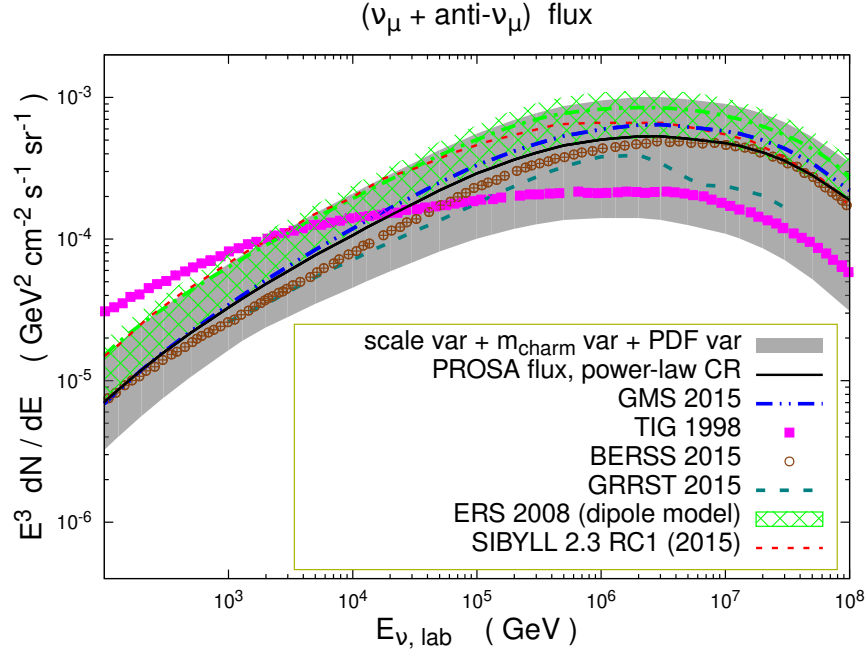
Figure 6: Predictions for prompt neutrino fluxes from this paper as compared to those by other authors [54, 64, 65, 69–71], using as a basis the same primary CR all-nucleon flux (BPL CR).
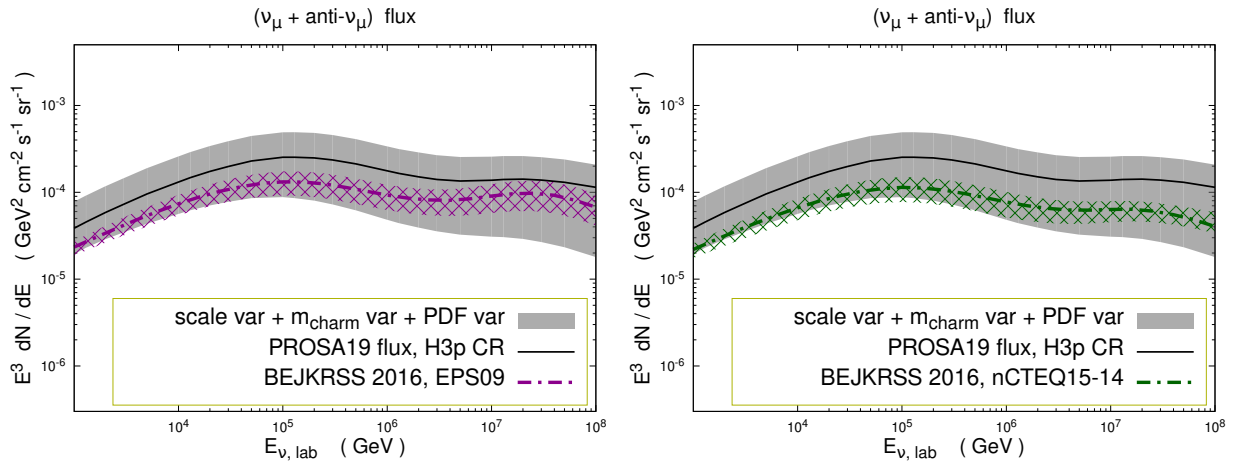

Figure 7: Predictions for prompt neutrino fluxes from this paper as compared to those by other authors [53], using as a basis the same all-nucleon flux (H3p CR) and two different nuclear PDFs for the description of the Nitrogen (air) target (EPS09 [72] and nCTEQ15 [73]).

References

[1] Y.L. Dokshitzer, Sov. Phys. JETP **46**, 641 (1977)

[2] V.N. Gribov, L.N. Lipatov, Sov. J. Nucl. Phys. **15**, 438 (1972)

[3] G. Altarelli, G. Parisi, Nucl. Phys. B **126**, 298 (1977). DOI 10.1016/0550-3213(77)90384-4

[4] G. Curci, W. Furmanski, R. Petronzio, Nucl. Phys. B **175**, 27 (1980). DOI 10.1016/0550-3213(80)90003-6

[5] W. Furmanski, R. Petronzio, Phys. Lett. B **97**, 437 (1980). DOI 10.1016/0370-2693(80)90636-X

[6] S. Moch, J.A.M. Vermaseren, A. Vogt, Nucl. Phys. B **688**, 101 (2004). DOI 10.1016/j.nuclphysb.2004.03.030

[7] A. Vogt, S. Moch, J.A.M. Vermaseren, Nucl. Phys. B **691**, 129 (2004). DOI 10.1016/j.nuclphysb.2004.04.024

[8] R. Aaij, et al., Nucl. Phys. **B871**, 1 (2013). DOI 10.1016/j.nuclphysb.2013.02.010

[9] R. Aaij, et al., JHEP **08**, 117 (2013). DOI 10.1007/JHEP08(2013)117

[10] O. Zenaiev, et al., Eur. Phys. J. **C75**(8), 396 (2015). DOI 10.1140/epjc/s10052-015-3618-z

[11] M.V. Garzelli, S. Moch, O. Zenaiev, A. Cooper-Sarkar, A. Geiser, K. Lipka, R. Placakyte, G. Sigl, JHEP **05**, 004 (2017). DOI 10.1007/JHEP05(2017)004

[12] S. Alekhin, et al., Eur. Phys. J. **C75**(7), 304 (2015). DOI 10.1140/epjc/s10052-015-3480-z. See `xfitter.org`

[13] H. Abramowicz, et al., Eur. Phys. J. **C75**(12), 580 (2015). DOI 10.1140/epjc/s10052-015-3710-4

[14] H. Abramowicz, et al., Eur. Phys. J. **C78**(6), 473 (2018). DOI 10.1140/epjc/s10052-018-5848-3

[15] R. Aaij, et al., JHEP **06**, 147 (2017). DOI 10.1007/JHEP06(2017)147

[16] R. Aaij, et al., JHEP **03**, 159 (2016). DOI 10.1007/JHEP03(2016)159,10.1007/JHEP09(2016)013,10.1007/JHEP05(2017)074. [Erratum: JHEP05,074(2017)]

[17] S. Acharya, et al., Eur. Phys. J. **C79**(5), 388 (2019). DOI 10.1140/epjc/s10052-019-6873-6

[18] S. Acharya, et al., Eur. Phys. J. **C77**(8), 550 (2017). DOI 10.1140/epjc/s10052-017-5090-4

[19] S. Alekhin. "OPENQCDRAD". See `http://www-zeuthen.desy.de/~alekhin/OPENQCDRAD/`

17

[20] A. Accardi, et al., Eur. Phys. J. **C76**(8), 471 (2016). DOI 10.1140/epjc/s10052-016-4285-4

[21] S. Alekhin, J. Blümlein, S. Moch, R. Placakyte, Phys. Rev. **D96**(1), 014011 (2017). DOI 10.1103/PhysRevD.96.014011

[22] R.D. Ball, V. Bertone, M. Bonvini, S. Marzani, J. Rojo, L. Rottoli, Eur. Phys. J. **C78**(4), 321 (2018). DOI 10.1140/epjc/s10052-018-5774-4

[23] H. Abdolmaleki, et al., Eur. Phys. J. **C78**(8), 621 (2018). DOI 10.1140/epjc/s10052-018-6090-8

[24] M. Dowling, S.O. Moch, Eur. Phys. J. **C74**(11), 3167 (2014). DOI 10.1140/epjc/s10052-014-3167-x

[25] F.D. Aaron, et al., Eur. Phys. J. **C59**, 589 (2009). DOI 10.1140/epjc/s10052-008-0792-2

[26] S. Chekanov, et al., JHEP **04**, 082 (2009). DOI 10.1088/1126-6708/2009/04/082

[27] P. Nason, C. Oleari, Nucl. Phys. **B565**, 245 (2000). DOI 10.1016/S0550-3213(99)00673-2

[28] S. Alekhin, K. Daum, K. Lipka, S. Moch, Phys. Lett. **B718**, 550 (2012). DOI 10.1016/j.physletb.2012.11.010

[29] K. Melnikov, A. Mitov, Phys. Rev. **D70**, 034027 (2004). DOI 10.1103/PhysRevD.70.034027

[30] M. Bonvini, F. Giuli, Eur. Phys. J. Plus **134**(10), 531 (2019). DOI 10.1140/epjp/i2019-12872-x

[31] F. James, M. Roos, Comput. Phys. Commun. **10**, 343 (1975). DOI 10.1016/0010-4655(75)90039-9

[32] S. Dulat, T.J. Hou, J. Gao, M. Guzzi, J. Huston, P. Nadolsky, J. Pumplin, C. Schmidt, D. Stump, C.P. Yuan, Phys. Rev. **D93**(3), 033006 (2016). DOI 10.1103/PhysRevD.93.033006

[33] L.A. Harland-Lang, A.D. Martin, P. Motylinski, R.S. Thorne, Eur. Phys. J. **C75**(5), 204 (2015). DOI 10.1140/epjc/s10052-015-3397-6

[34] J. Pumplin, D. Stump, R. Brock, D. Casey, J. Huston, J. Kalk, H.L. Lai, W.K. Tung, Phys. Rev. D **65**, 014013 (2001). DOI 10.1103/PhysRevD.65.014013

[35] M. Tanabashi, et al., Phys. Rev. **D98**(3), 030001 (2018). DOI 10.1103/PhysRevD.98.030001

[36] H1 and ZEUS Collaborations, JHEP **01**, 109 (2010). DOI 10.1007/JHEP01(2010)109

[37] V. Bertone, S. Carrazza, J. Rojo, Comput. Phys. Commun. **185**, 1647 (2014). DOI 10.1016/j.cpc.2014.03.007

[38] S. Forte, E. Laenen, P. Nason, J. Rojo, Nucl. Phys. **B834**, 116 (2010). DOI 10.1016/j.nuclphysb.2010.03.014

18

[39] V. Bertone, et al., Eur. Phys. J. **C77**(12), 837 (2017). DOI 10.1140/epjc/s10052-017-5407-3

[40] S. Chekanov, et al., Phys. Lett. **B547**, 164 (2002). DOI 10.1016/S0370-2693(02)02763-6

[41] S. Chekanov, et al., Nucl. Phys. **B765**, 1 (2007). DOI 10.1016/j.nuclphysb.2006.09.018

[42] H. Abramowicz, et al., Eur. Phys. J. **C70**, 965 (2010). DOI 10.1140/epjc/s10052-010-1504-2

[43] A. Aktas, et al., Phys. Lett. **B653**, 134 (2007). DOI 10.1016/j.physletb.2007.07.050

[44] F.D. Aaron, et al., Eur. Phys. J. **C67**, 1 (2010). DOI 10.1140/epjc/s10052-010-1282-x

[45] S. Chatrchyan, et al., Phys. Rev. **D87**(11), 112002 (2013). DOI 10.1103/PhysRevD.87.112002,10.1103/PhysRevD.87.119902. [Erratum: Phys. Rev.D87,no.11,119902(2013)]

[46] A.M. Sirunyan, et al., Eur. Phys. J. **C77**(7), 459 (2017). DOI 10.1140/epjc/s10052-017-4984-5

[47] A.M. Sirunyan, et al., Submitted to: Eur. Phys. J. (2019)

[48] T.K. Gaisser, R. Engel, E. Resconi, *Cosmic Rays and Particle Physics* (Cambridge University Press, 2016). URL http://www.cambridge.org/de/academic/subjects/physics/cosmology-relativity-and-gravitation/cosmic-rays-and-particle-physics-2nd-edition?format=HB

[49] M. Ageron, et al., Nucl. Instrum. Meth. **A656**, 11 (2011). DOI 10.1016/j.nima.2011.06.103

[50] T. Gaisser, F. Halzen, Ann. Rev. Nucl. Part. Sci. **64**, 101 (2014). DOI 10.1146/annurev-nucl-102313-025321

[51] S. Adrian-Martinez, et al., J. Phys. **G43**(8), 084001 (2016). DOI 10.1088/0954-3899/43/8/084001

[52] C. Mascaretti, F. Vissani, JCAP **1908**(08), 004 (2019). DOI 10.1088/1475-7516/2019/08/004

[53] A. Bhattacharya, R. Enberg, Y.S. Jeong, C.S. Kim, M.H. Reno, I. Sarcevic, A. Stasto, JHEP **11**, 167 (2016). DOI 10.1007/JHEP11(2016)167

[54] M.V. Garzelli, S. Moch, G. Sigl, JHEP **10**, 115 (2015). DOI 10.1007/JHEP10(2015)115

[55] T.K. Gaisser, Astropart. Phys. **35**, 801 (2012). DOI 10.1016/j.astropartphys.2012.02.010

[56] T.K. Gaisser, T. Stanev, S. Tilav, Front. Phys.(Beijing) **8**, 748 (2013). DOI 10.1007/s11467-013-0319-7

[57] V.P. Goncalves, R. Maciula, R. Pasechnik, A. Szczurek, Phys. Rev. **D96**(9), 094026 (2017). DOI 10.1103/PhysRevD.96.094026

[58] P. Nason, JHEP **11**, 040 (2004). DOI 10.1088/1126-6708/2004/11/040

[59] S. Frixione, P. Nason, G. Ridolfi, JHEP **09**, 126 (2007). DOI 10.1088/1126-6708/2007/09/126

[60] T. Sjöstrand, S. Ask, J.R. Christiansen, R. Corke, N. Desai, P. Ilten, S. Mrenna, S. Prestel, C.O. Rasmussen, P.Z. Skands, Comput. Phys. Commun. **191**, 159 (2015). DOI 10.1016/j.cpc.2015.01.024

[61] M. Benzke, M.V. Garzelli, B. Kniehl, G. Kramer, S. Moch, G. Sigl, JHEP **12**, 021 (2017). DOI 10.1007/JHEP12(2017)021

[62] T. Kneesch, B.A. Kniehl, G. Kramer, I. Schienbein, Nucl. Phys. **B799**, 34 (2008). DOI 10.1016/j.nuclphysb.2008.02.015

[63] M.G. Aartsen, et al., Astrophys. J. **833**(1), 3 (2016). DOI 10.3847/0004-637X/833/1/3

[64] P. Gondolo, G. Ingelman, M. Thunman, Astropart. Phys. **5**, 309 (1996). DOI 10.1016/0927-6505(96)00033-3

[65] R. Enberg, M.H. Reno, I. Sarcevic, Phys. Rev. **D78**, 043005 (2008). DOI 10.1103/PhysRevD.78.043005

[66] S. Thoudam, J.P. Rachen, A. van Vliet, A. Achterberg, S. Buitink, H. Falcke, J.R. Hörandel, Astron. Astrophys. **595**, A33 (2016). DOI 10.1051/0004-6361/201628894

[67] H.P. Dembinski, R. Engel, A. Fedynitch, T. Gaisser, F. Riehn, T. Stanev, PoS **ICRC2017**, 533 (2018). DOI 10.22323/1.301.0533. [35,533(2017)]

[68] S. Alekhin, J. Blumlein, S. Moch, Phys. Rev. **D86**, 054009 (2012). DOI 10.1103/PhysRevD.86.054009

[69] A. Bhattacharya, R. Enberg, M.H. Reno, I. Sarcevic, A. Stasto, JHEP **06**, 110 (2015). DOI 10.1007/JHEP06(2015)110

[70] R. Gauld, J. Rojo, L. Rottoli, S. Sarkar, J. Talbert, JHEP **02**, 130 (2016). DOI 10.1007/JHEP02(2016)130

[71] A. Fedynitch, R. Engel, T.K. Gaisser, F. Riehn, T. Stanev, EPJ Web Conf. **99**, 08001 (2015). DOI 10.1051/epjconf/20159908001

[72] K.J. Eskola, H. Paukkunen, C.A. Salgado, JHEP **04**, 065 (2009). DOI 10.1088/1126-6708/2009/04/065

[73] K. Kovarik, et al., Phys. Rev. **D93**(8), 085037 (2016). DOI 10.1103/PhysRevD.93.085037

A Additional studies of gluon parametrisation

To ensure that the gluon PDF at low x is not overconstrained in the fit, different functional forms in the parametrisation are tested, as used in the ABMP16 [21], CT14 [32], HERAPDF2.0 [13] and Bonvini-Giuli (BG) [30] PDF fits:

$$
\begin{aligned}
\text{ABMP16:} \quad & xg(x) = A(1-x)^b x^{a(1+\gamma_1 x)}, \\
\text{CT14:} \quad & xg(x) = A x^{a_1}(1-x)^{a_2}(e_0(1-y)^2 + e_1(2y(1-y)) + y^2), y = 2\sqrt{x} - x, \\
\text{HERAPDF2.0:} \quad & xg(x) = A_g x^{B_g}(1-x)^{C_g} + A'_g x^{B'_g}(1-x)^{25}, \\
\text{HERAPDF2.0 no flex. } g: \quad & xg(x) = A_g x^{B_g}(1-x)^{C_g}, \\
\text{BG:} \quad & xg(x) = A_g x^{B_g}(1-x)^{C_g}(1 + F_g \log x + G_g \log^2 x),
\end{aligned}
\tag{4}
$$

These functional forms are characterised by 3 (HERAPDF2.0 no flex. g), 4 (ABMP16), 5 (CT14, HERAPDF2.0, BG) or 7 (MMHT2014) parameters controlling the gluon PDF, c.f. 4 parameters in the presented nominal parametrisation of Eq. (1). The resulting gluon distributions are presented in Fig. 8. The parametrisations of ABMP16, HERAPDF2.0 without the flexible gluon, and BG provide very similar results to that of the nominal parametrisation in Eq. (1). Note that also the HERAPDF2.0 analysis considered the parametrisation without the flexible gluon, stamped it as 'alternative' gluon parameterisation [13] and provided primarily for predictions of cross sections at very low x, such as very high-energy neutrino cross sections.

The fit using the HERAPDF2.0 and CT14 parametrisations yielded a gluon distribution with a sharp turnover to negative values at $x \sim 10^{-6}$, i.e. at the edge of the kinematic reach of the used measurements. Using such PDFs would lead to a negative prediction for the total charm hadroproduction cross sections at $\sqrt{s} \gtrsim 20$ TeV, similar to the observation of Ref. [20]. Therefore these parametrisations are discarded (despite they provide an improved χ^2, by 22 and 7 units when using the HERAPDF2.0 and CT14 parametrisations, respectively). In this analysis, it was not possible to achieve convergence of the fit using the MMHT2014 parametrisation [33], because of no essential sensitivity of the used data sets to the gluon distribution at high x.

The gluon distribution obtained in the fit using different parametrisations, see Eq. (4) are shown on Fig. 8.
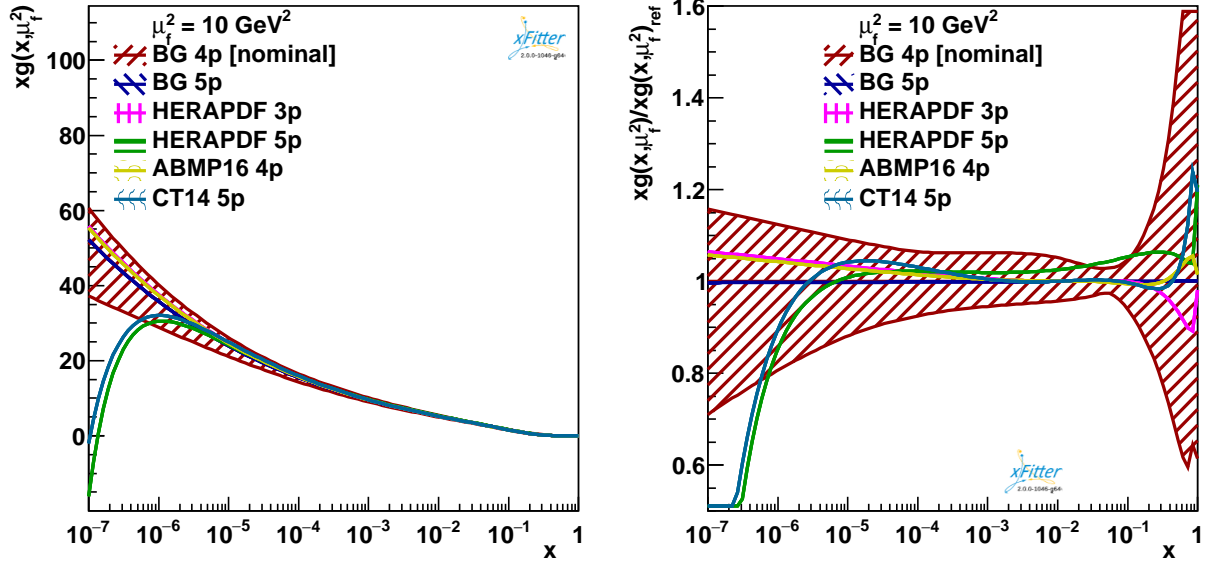
Figure 8: (left) The gluon PDF with their total uncertainties at the scale $\mu_f^2 = 10$ GeV^2 obtained using different gluon parametrisations, see Eq. (4). (right) The same PDFs normalised to the distribution obtained using the nominal parametrisation.